Highlights

Modeling PDC cutter - rock interactions using the finite discrete element method for geothermal drilling applications

Erin Heilman, Bryan Euser, Luke Frash, Meng Meng, Wenfeng Li, Zhou Lei, Ryan Rhodes, Allison Kimbrough, Esteban Rougier

- Simulated polycrystalline diamond compact cutter-rock interaction using finite discrete element method code.
- Explored the effects of drilling parameters on cutting force and compared them with laboratory-obtained values.
- Replicated drilling conditions using a 3-D numerical model of fracture propagation under confining pressure.

Modeling PDC cutter - rock interactions using the finite discrete element method for geothermal drilling applications

Erin Heilman[a], Bryan Euser[a], Luke Frash[b], Meng Meng[b], Wenfeng Li[b], Zhou Lei[a], Ryan Rhodes[c], Allison Kimbrough[c], Esteban Rougier[a]

[a]*National Security Earth Science Los Alamos National Laboratory Los Alamos New Mexico*
[b]*Energy and Natural Resources Security Los Alamos National Laboratory Los Alamos New Mexico*
[c]*Oxy Houston Texas*

Abstract

Polycrystalline diamond compact (PDC) cutters are used in geothermal energy drilling operations as they are exceptionally effective due to their strength and resistance to abrasion. It is important to understand the effect of downhole conditions to accurately model rock-cutter-rock interactions, as well as wear on the bit and drilling efficiency. Cutting efficiency is determined through the weight on the bit, rotational speeds, and other cutter and rock parameters in drilling, here we can comment on cutting efficiency through the cutting force. The ultimate goal of this research is to numerically model the PDC cutter–rock interaction in 3-D to find an optimal arrangement of parameters for efficient geothermal drilling. Using the combined finite discrete element method (FDEM), we model rock fracture and fragmentation for a single PDC cutter for both atmospheric and realistic well pressure conditions. We present the numerical analysis progression of PDC cutter-rock interaction in 2-D and 3-D for a range of cutting speeds, depth of cuts, and pressures using sandstone and granite as our rock materials. These parameters are varied to understand the optimal configuration to increase drilling performance as determined by cutting force, damage style, and fracture energy. Our models successfully reproduce laboratory values, which increases our understanding of rock fracture at downhole conditions.

Keywords: finite discrete element method, polycrystalline diamond compact cutter, numerical modeling, fracture mechanics, geothermal

1. Introduction

Geothermal energy has become an increasingly viable form of energy in the United States and other parts of the world. Geothermal energy typically targets deep, hot, hard rock sources, which differ from conventional/unconventional oil and gas targets [1, 2]. Geothermal drilling targets present additional challenges because the downhole confining pressures, temperatures, and stresses are higher, which in turn reduces drilling efficiency [3]. Drilling efficiency is determined by the rate of penetration (ROP) that a drill bit can achieve [4]. A commonly used drill bit is the polycrystalline diamond compact (PDC) cutter bit [5, 6], due to its strength and resistance to abrasive wear. PDC bits are primarily used for rock cutting and typically shear rock to break it, however, many parameters can affect the fracture process of the rock during drilling. Investigating the rock-breaking process in geothermal energy drilling and the effects of the drill bit is essential to increase performance and reduce the overall cost of the drilling, which can be over half of the total project cost [7]. One way to investigate rock-breaking processes is through accurate numerical modeling, which allows us to understand the fracture processes in geothermal target rocks and the cutter response to various drilling parameters.

The effect of cutter wear on cutting performance is a key question in geothermal drilling. As a drill bit cuts for extended periods of time, the PDC cutters will become worn from constant use, otherwise known as a wear flat. This wear flat reduces the contact area of the cutter. Deciding when or how often to replace worn drill bits is challenging, as it is time consuming and expensive to retract the drill and change out bits [8]. Worn PDC cutters tend to lead to reduced ROP, even with a small amount of wear [9]. Understanding the dynamics behind the reduced efficiency due to wear flats would be a great benefit for drilling operations.

To model geothermal drilling, we first simplify the model of the problem to gain a basic understanding of the cutter-rock system. Though drill bits consist of many PDC cutters arranged at different angles on it; in this work, we model a singular PDC cutter and its interaction with the rock to understand the mechanisms and forces controlling rock fracture. In a geothermal drilling setting, the operator controls the revolutions per minute (RPM) of

the drill bit and the weight on bit (WOB). In our numerical models, we prescribe the velocity of the cutter and the depth of the cut to approximate these factors.

Many numerical modeling methods can model rock fracture and have been used to model cutter-rock interaction. [10] used the finite element method to model both 2-D and 3-D cases of rock cutting and compared with observed laboratory data. [11] used the discrete element method, specifically a modified bonded-particle model, in their cutter-rock model which revealed a crush zone below the chamfer edge on the cutter and a shear zone ahead of the cutting face. Several authors have utilized the finite discrete element method (FDEM) for fracture and damage modeling, which combines the two previously mentioned methods, as it replicates realistic fracture and fragmentation of the rock [12, 13, 14, 15, 16, 17].

FDEM has been used to investigate cutter-rock interactions before, though few studies have investigated this interaction in 3-D or modeled these interactions with confining pressure. These additions are necessary to model realistic settings in order to extrapolate results to geothermal drilling. We utilize the Hybrid Optimization Software Suite (HOSS), an FDEM code [12], to model PDC cutter-rock interaction in both 2-D and 3-D. This work is used as benchmarking for this cutter-rock interaction and explores expanded capabilities related to a geothermal energy drilling setting.

2. Numerical Method and Material Properties

2.1. Finite discrete element method

FDEM can model both finite-element continuum behavior and discontinuous mechanical behavior [18, 19, 20]. This allows one to model fracture and fragmentation of initially intact, continuous materials. The governing equation of the displacement $\mathbf{x}$ of a node in the numerical domain can be described as

$$\mathbf{M}\frac{d^2\mathbf{x}}{dt^2} + \mathbf{C}\frac{d\mathbf{x}}{dt} + \mathbf{K}\mathbf{x} = \mathbf{f}, \tag{1}$$

where $\mathbf{M}$ is the mass matrix, $\mathbf{C}$ is the damping matrix, $\mathbf{K}$ is the stiffness matrix, and $\mathbf{f}$ is the force on a node. An explicit, second-order, central difference time integration scheme is used to obtain the temporal evolution of the system [21]. The numerical domain is discretized with triangular elements

in 2-D, and tetrahedral elements in 3-D. Cohesive bonds are inserted between all adjacent element pairs. Failure of these bonds can be used to represent discrete fracture processes.

The constitutive behavior of cohesive bonds is described as a function of relative displacement between opposing element boundaries (e.g., element edges in 2-D, element faces in 3-D). Failure of a cohesive bond initiates once specific failure criteria are met. Mode I, or tensile, fracture initiates when the tensile strength σ_{n} of the cohesive bond is exceeded. Similarly, Mode II, or in-plane shear, fracture initiates when the tangential strength σ_{t} of the bond is exceeded. Mode II fracture is governed by a Mohr-Coulomb failure criterion

$$\tau = \sigma \tan \phi + c \tag{2}$$

where τ is the shear strength, c is the cohesion, σ is the normal stress acting on the cohesive bond, and ϕ is the internal angle of friction. Cohesive bonds can fail in mode I, mode II, or some combination of mode I and II (i.e., mixed mode) [14]. Cohesive bonds undergoing failure exhibit displacement-based softening behavior. That is, after the onset of failure, as the bond undergoes continuous displacement, it weakens and dissipates energy [18]. Once a bond reaches a maximum opening displacement, it immediately breaks, generating a new fracture surface in the numerical domain.

2.2. Calibration

It is necessary to calibrate the micro-physical parameters used in the numerical model from tested rock measurements. Following the method outlined by [22], we carry out both Brazilian Disc (BD) and Uniaxial Compressive Stress (UCS) tests in 2-D. For the rock material, we used properties of Vosges sandstone (see Table 1) as it has published experimental measurements and rock scratch test data, allowing for verification of our models [23, 24]. We use experimentally measured values as reference in our calibration method. To calibrate our numerical model to the experimental observations, we adjust the maximum cohesive bond displacements and the angle of internal friction. Note that the remaining material properties used in the models, i.e., density, stiffness, tensile and shear strength, and Poisson's ratio are taken directly from experimental measurements.

In the BD test, we have two non-deforming plates on the top and bottom of a circular rock specimen with a diameter of 50.8 mm. The top plate, with a fixed velocity of 0.1 m/s, compresses the specimen while the bottom plate

Table 1: Rock Material Properties as used in HOSS [24, 10]

Properties	Vosges Sandstone	FORGE Granite
Young's Modulus / GPa	8.3	48.26
UCS / MPa	42	211
Tensile Strength, σ_n / MPa	2.9	10.62
Cohesion, σ_t / MPa	11.545	44.815
Density / (kg/m^3)	2075	2610
Internal angle of friction, ϕ / deg	26.6	38.6
Poisson's Ratio	0.3	0.23
Mode I fracture energy / (J/m^2)	8.7	15.9
Mode II fracture energy / (J/m^2)	34.6	67.2

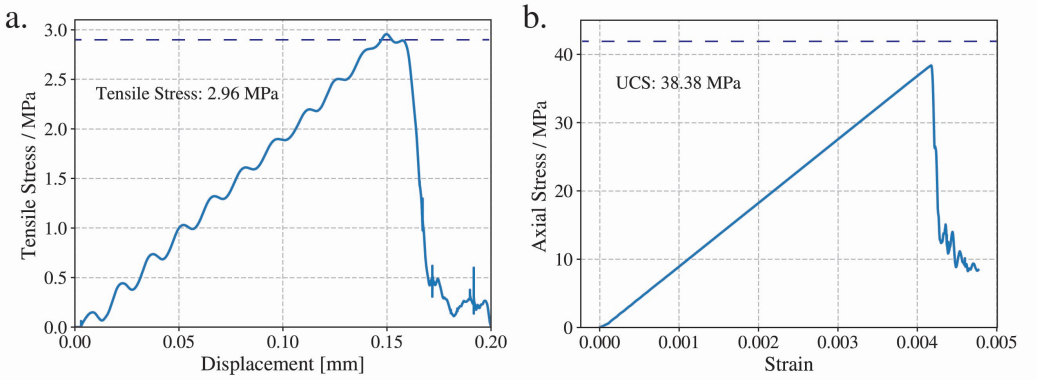

Figure 1: Plots of a.) BD test and b.) UCS showing calibrated values with dashed lines showing laboratory measured values [23, 24]

remains stationary. The UCS test has a similar setup with a rectangular block, with a length-to-width ratio of 2:1, between two plates. In this case, the top plate moves with a fixed velocity of 0.1 m/s while the bottom plate remains stationary. In both tests, the moving plate increases stress in the material until it reaches a peak stress, which subsequently drops as failure occurs.

Figure 1 shows the results of the calibration tests. The BD test has an error of 2.06% when comparing the numerical value of 2.96 MPa to the measured value of 2.9 MPa [23], while the UCS test has an error of 8.62% when comparing the numerical value of 38.38 MPa to the measured value of 42 MPa [24]. Our numerical values are within an acceptable range of the

measured values, so we use the values listed in Table 1 for our numerical modeling.

3. Model Setup

We first run models in 2-D and then in 3-D to understand the effects of cutter velocity, depth of cut, and confining pressure. A suite of 2-D models is run first to find the optimal configuration of variables because the 2-D models are more computationally efficient than the 3-D models. The 2-D model setup (Figure 2a) consists of a slanted rectangular 2 mm x 13 mm PDC cutter moving at a prescribed constant velocity with a prescribed depth of cut. The edge of the PDC cutter has a 45° chamfer in both the 2-D and 3-D models. The cutter moves through a rock specimen 38.4 mm x 19.5 mm in height and width, respectively. The specimen is notched, with the depth of the notch being equal to the depth of cut. The specimen is notched in order to reduce nonphysical stresses that can arise in the initial phase of cutting. The average mesh sizes of the cutter and specimen are 0.5 mm and 0.25 mm, respectively. The measured grain size of Vosges sandstone ranges from 0.1 mm to 0.3 mm [23], making our mesh size an accurate representation the material. The 3-D model is an extension of the 2-D model(see Figure 2b), where the bottom remains fixed and the other sides of the box are roller boundary conditions (i.e., displacement is restricted in the direction normal to the boundary). For these models, we modify the rock specimen to have a lateral extent of 30 mm to limit unrealistic edge effects. The 3-D mesh coarsens with increasing distance from the cutter to optimize computational efficiency. The PDC cutter is represented as a disc with a diameter of 13 mm and a thickness of 2.5 mm.

A fixed velocity boundary condition is imposed on the bottom of the specimen. The left and right sides of the specimen are given roller boundary conditions. The cutter is treated as a rigid body (i.e., the cutter is not deformable) with a constant velocity. In practice, a cutter will wear the longer it is used, however we only model a few millimeters of displacement, making the rigid body assumption reasonable. Both the cutter velocity and depth of cut are varied in our 2-D tests. The cutter is prescribed velocities of 1 m/s, 4 m/s, and 10 m/s and cutting depths of 0.3 mm, 1.2 mm, and 3.6 mm. We impose a back rake angle of 20° for the PDC cutter, which has been previously suggested as optimal for geothermal drilling [25]. We measure the cutting force on the PDC cutter to compare model results against experi-

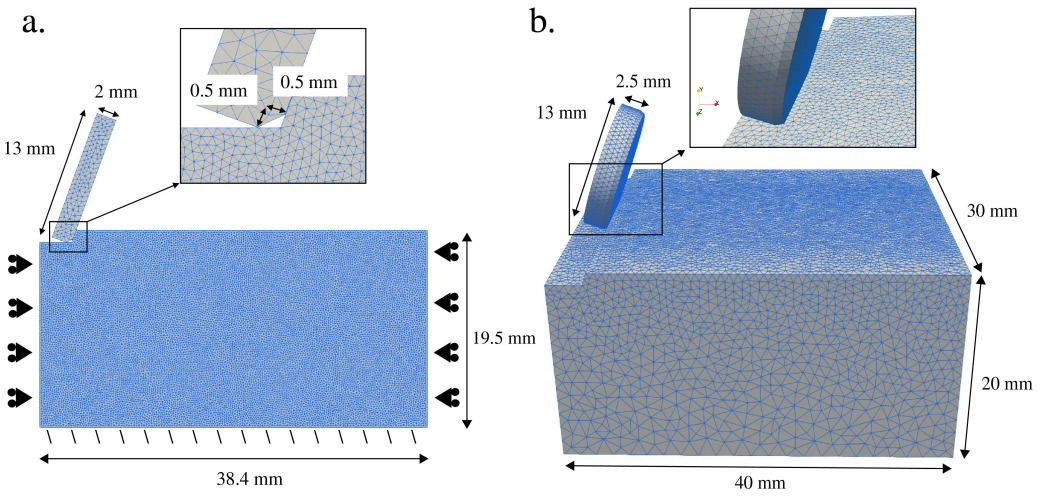

Figure 2: a.) 2-D model setup showing cutter with chamfered edge and rock block dimensions. The nodes on the bottom of the block are fixed in space, while the nodes on the two sides of the block are allowed to slide in the y direction. b.) 3-D model setup showing cutter with chamfered edge and rock block dimensions

mental observations. We also perform statistical analysis on the simulated fractures.

We also include results from both 2-D and 3-D simulations that incorporate confining pressure conditions. We mimic pressures that occur in geothermal energy drilling by applying vertical and horizontal confining pressures. In our simulations, a vertical confining pressure of 30.29 MPa, which represents the hydrostatic pressure due to the drill mud column at roughly 5,000 ft drilling depth, is applied, while a horizontal confining pressure of 17.85 MPa, representing the in-situ stress conditions in the rock formation, is applied to the left boundary.

Lastly, we model cutter wear in 3-D in granite under *in-situ* pressure conditions. The granite properties come from Utah FORGE site collected data [26]. For our models of cutter wear, three discrete levels of wear are tested. The levels of cutter wear are 0.174 mm, 0.429 mm, and 0.684 mm measured as the depth removed from the bottom of the cutter (parallel to the cutting surface) as seen in Figure 3. The largest cutter wear represents wearing through the entire PDC cutter to the steel casing. These wear flats are held in the same y-position as the sharp cutter to accurately reflect the loss in contact area the wear flat represents. We measure the stress on the

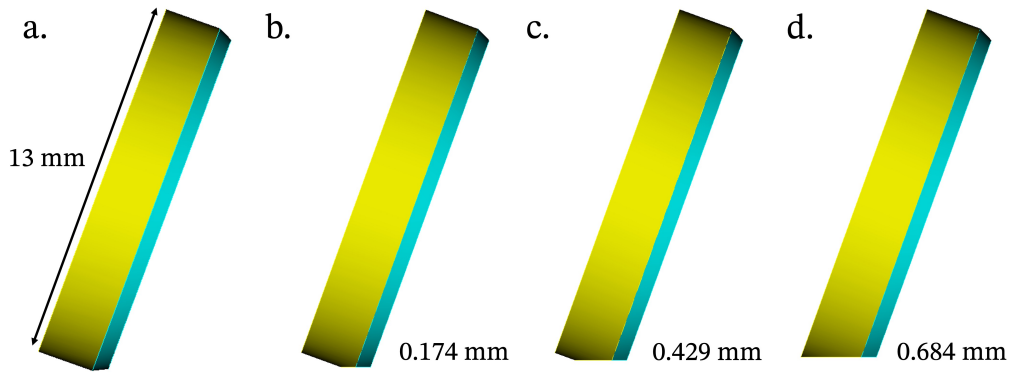

Figure 3: a.) The sharp chamfer PDC cutter compared to: b.) the small wear flat (0.174 mm), c.) the medium wear flat (0.429 mm), and d.) the large wear flat (0.684 mm).

cutter, the cutting forces, and the rock fracture and fragmentation patterns in our models to understand the forces on the cutters and how they contribute to wear.

4. Model Results

For model validation, we compare our modeled cutting forces to rock scratch test data collected on Vosges sandstone [24]. As in [10], we compare data from models with 4 m/s cutting velocity, as it reasonably compares to laboratory data that had a cutting velocity of roughly 4 mm/s. Figure 4a and 4b shows these comparisons for depths of cut of 0.3 mm and 3.6 mm, respectively. The modeled cutting forces are on the same order of magnitude as the experimental data. The experimental data was collected during continuous scratching and exhibits continuous cutting force. When the cutter is contacting in the numerical models we observe similar values of cutting force.

4.1. Cutting Forces

We plot the x-component of the cutting force, i.e., in the direction that the cutter moves, for the various cutter velocities, first showing the 2-D model results. Figure 5 shows the cutting force for the 2-D models with three cutting depths with cutter velocities of 1 m/s, 4 m/s, and 10 m/s, respectively. The cutting forces for the 3.6 mm depth of cut are consistently the highest when compared to those at other cutting depths. At 0.3 and

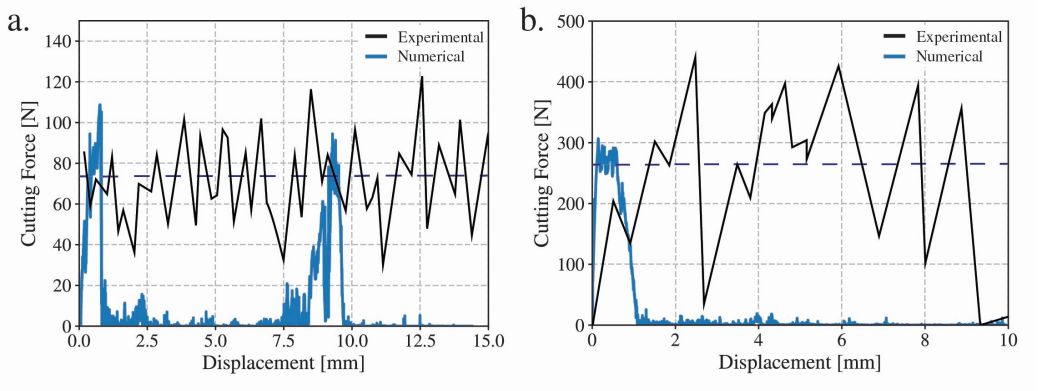

Figure 4: Plot of cutting forces for experimental data and numerical results at depth of cut of a.) 0.3 mm at velocity 4 m/s and b.) 3.6 mm at velocity 4 m/s, with experimental data taken from [10]. The horizontal dashed line shows the average cutting force measured during the experiment.

1.2 mm cutting depths, the cutting force is similar across the different cutter velocities. At all depths, the cutting force increases as the cutter velocity increases. For all cases, the cutting force decreases to zero when the cutter loses contact with the rock specimen. In Figure 5b and c, the cutting force peaks again after decreasing to zero, this occurs when the cutter resumes contact with the rock specimen. The decrease in cutting force to zero when contact is lost is typical for numerical modeling of a single cutter [27]. As the cutter velocity increases, the overall time in contact increases along with the total displacement. The models with a cutter velocity of 10 m/s have the most time in contact between the cutter and rock specimen. There is also a slight increase in peak cutting forces with the increase in cutter velocity.

In comparison, Figure 5 d, e, and f show the same 2-D cases with confining pressure applied. In all cases for the confining pressure models, the cutting force is higher than the non-pressure models. When the rock specimen fragments, there is a corresponding drop in the cutting force; however, due to the applied confining pressure, the cutter does not lose contact with the rock and the cutting force does not drop to zero. When the depth of cut is 0.3 mm, the cutter is constantly contacting the rock as it scrapes, resulting in a relatively steady cutting force with visible chatter.

We extended the models to three dimensions to better capture the complexity of the cutting dynamics. For the 3-D tests, the depth of cut is 1.2 mm and the cutter velocity is 4 m/s, the model is run both with and without con-

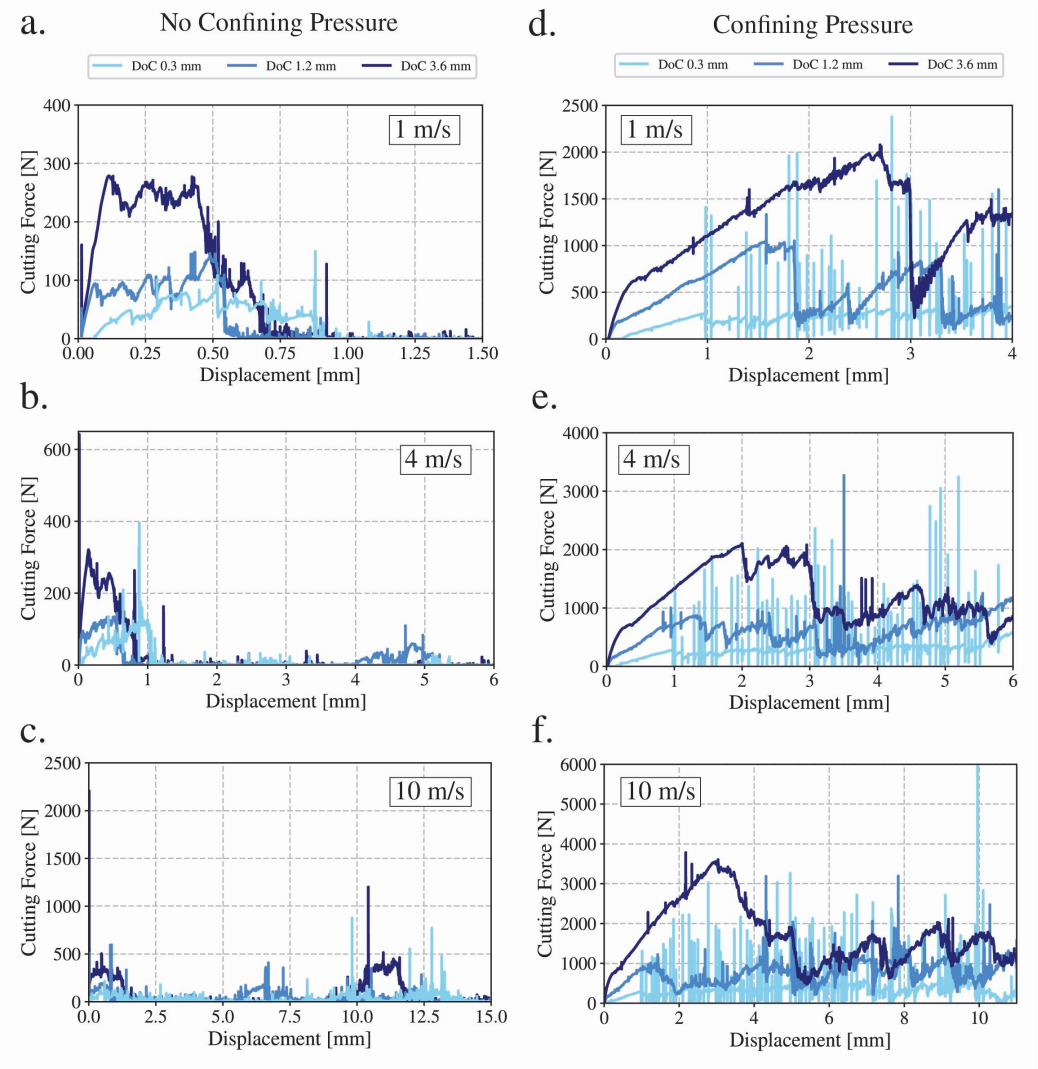

Figure 5: Plot of cutting force in x-direction for no confining pressure 2-D cases a.) 1 m/s, b.) 4 m/s, and c.) 10 m/s cutter velocity cases and d.) 1 m/s, e.) 4 m/s, and f.) 10 m/s for the 2-D confining pressure models.

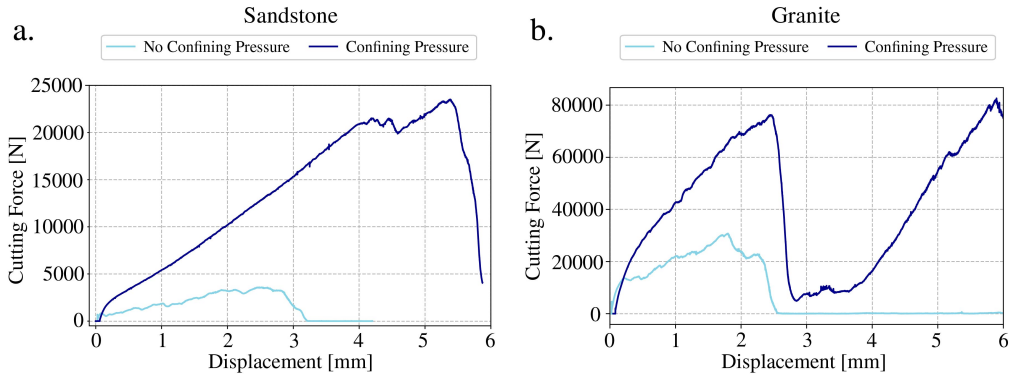

Figure 6: Comparison of cutting forces of the 3-D models for a.) sandstone and b.) granite.

fining pressure.

Figure 6 compares the cutting forces between 3-D models for the sandstone and granite materials. Figure 6a shows the sandstone models where the maximum cutting force of the model without confining pressure is 3500 N, while the maximum cutting force of the model with confining pressure is 23500 N, a 20000 N increase. Not only does the model with confining pressure exhibit higher cutting forces, but the pressurized model also requires approximately 3 mm more displacement to reach its maximum cutting force. This difference is consistent with the results of the 2-D tests in that the pressurized model has a higher cutting force and requires more displacement to reach its maximum value.

Figure 6b shows the 3-D cutting force results for the granite, which are roughly an order of magnitude higher than the sandstone. This discrepancy is due to the difference in tensile and shear strengths between the materials. Here, the granite model without confining pressure peaks to around 30000 N while the confining pressure model peaks to sim80000 N. As observed previously, the cutting force in the pressurized model does not drop to zero after reaching its peak.

Figures 7a and 7b compare the cutting forces of various wear flats to those of a sharp cutter in granite, under conditions with no confining pressure and with confining pressure, respectively. Both the small and medium wear flats produce higher cutting forces than the sharp cutter under both pressure conditions. Additionally, these wear flats reach their peak cutting forces at greater displacements. When comparing the flats, the medium wear flat

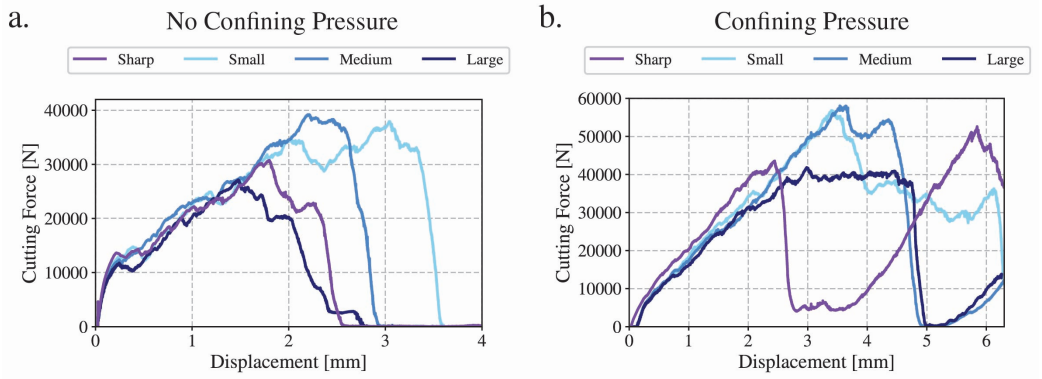

Figure 7: Comparison of cutting forces of the 3-D models with wear flats versus sharp cutter a.) without confining pressure and b.) with confining pressure.

exhibits the highest cutting force at the greatest displacement, whereas the largest wear flat produces the smallest peak force. Figure 7a shows that all wear flat cases and the sharp cutter exhibit roughly the same trend in the cutting force. Figure 7b illustrates the effect of confining pressure on the observed cutting forces. The small wear flat exhibits a gradual decline after peaking, the medium wear flat develops a second peak before a sharp drop, and the large wear flat sustains the peak cutting force for approximately 2 mm before decreasing. Interestingly, the cutting force produced by both the medium and large wear flats drops to zero after peaking, which may be related to the reduced contact area of the cutter.

4.2. Damage and Fracture Energy Calculations

We present results elucidating the damage behavior of our models. In order to do so we first extracted the model data and selected the element edges (in 2-D) and element faces (in 3-D) that had damage of 1, i.e. elements that are fully damaged. We then constructed histograms to classify the type of damage the edge or face underwent. The types of damage an element can undergo are pure tension (Mode 1), pure shear (Mode 2), or mixed-mode, which is some combination of shear and tensile damage. The histograms are normalized by weight and binned by damage type, the y-axis counts represent the percentage of that damage type compared to the total number of fully damaged elements. In our histograms, pure shear is 0, pure tension is 1, and mixed-mode is in between 0 and 1.

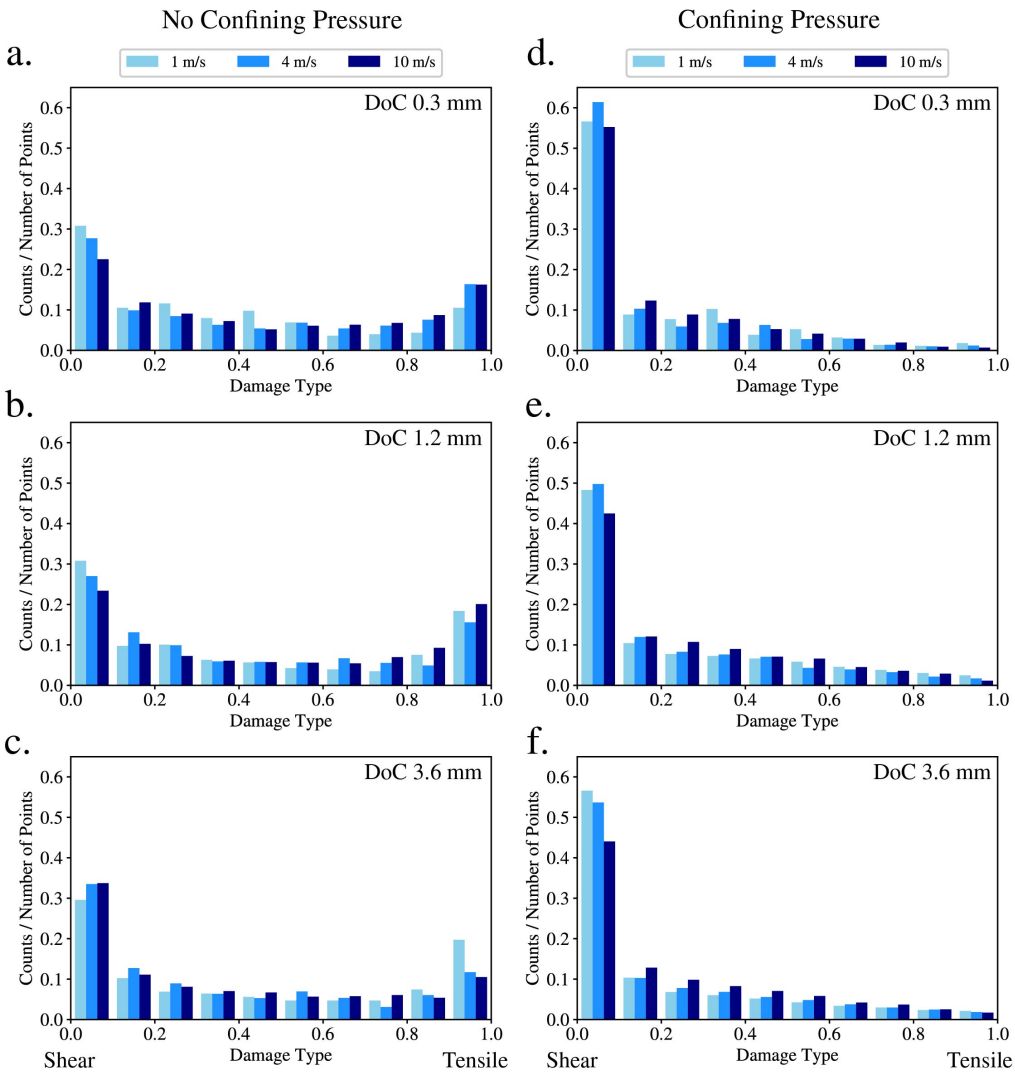

Figure 8: Comparison of 2-D models showing histograms of completely damaged elements, binned by damage type, for the sharp cutter. a.) and d.) show the depth of cut of 0.3 mm for no confining pressure and confining pressure, respectively, b.) and e.) show the depth of cut of 1.2 mm for no confining pressure and confining pressure, and c.) and f.) show the depth of cut of 3.6 mm for no confining pressure and confining pressure.

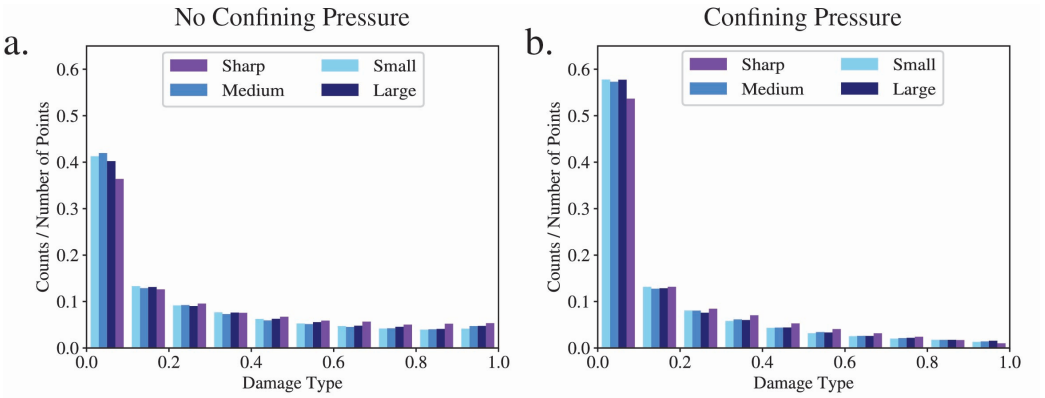

Figure 9: Histograms of the completely damaged elements from the 3-D granite models histograms, binned by damage type. a.) shows comparison of sharp cutter and wear flats without confining pressure b.) shows comparison of sharp cutter and wear flats with confining pressure.

Figure 8 shows the damage histogram for all of the 2-D models of the sharp cutter separated by depth of cut and confining pressure. We see that the models are dominated by shear damage, due to the cutting style of PDC cutters, which is even more evident in the cases with confining pressure. In cases with no confining pressure, increasing cutting depth and cutter speed does not strongly affect the proportion of shear damage (Figure 8a, b, and c). In the cases with confining pressure, there is no significant change in the amount of shear damage, but the amount of mixed-mode damage increases with cutting depth (Figure 8d, e, and f). The cases with no confining pressure tend to have more pure tensile damage, approximately 20%, than the pressurized cases that have almost no pure tensile damage.

We also quantify the damage in the 3-D granite wear flat studies for (a.) no confining pressure and (b.) confining pressure conditions (b.) in Figure 9. For both conditions, the sharp cutter produces less pure shear damage than the wear flats. The mixed-mode damage produced is relatively equal across sharp and wear flat cutters. Similar to our 2-D results, the no confining pressure models have more pure tensile damage than the pressurized models, however, the amount of tensile damage is very small overall (less than 10%). All confining pressure models have roughly 20% more pure shear damage than the no confining pressure models. This trend points towards shearing and crushing mechanisms under confining pressure as opposed to cracking

the rock.

Next, we wanted to quantify the energy required to fracture rock. First we needed to calculate the area of the fractured rock. We used the previously extracted, fully damaged element data to calculate the area of the damage. In 3-D, the 'area' is the face of the damaged element, here we utilize tetrahedrons in our 3-D mesh so the element face is a triangle. Next, we need to know the proportion of the damage modes used in fracturing that element. In some cases, an element is damaged by pure shear or pure tension, as we previously saw from the histograms, but we must accurately account for mixed-mode damage as well. So we calculate what portion of tensile or shear damage the element experienced, and this proportion goes into the stress calculation for the energy. Now that we know the area and the stress of the damage we can calculate the fracture energy. Equation 3 shows the calculation of fracture energy,

$$E = \frac{\sum A(\sigma_s \%\sigma_s + \sigma_t \%\sigma_t)\delta}{2}, \tag{3}$$

where E is the total fracture energy in Joules, A is the area of a single element face, σ_s is the shear stress, $\%\sigma_s$ is the proportion of shear damage, σ_t is the tensile stress, $\%\sigma_t$ is the proportion of tensile damage, and δ is the displacement allowed between cohesive bonds before failure. This calculation is repeated for every fully damaged element face, summed, then divided by two so as to not count each face twice and the result was the fracture energy for the fully damaged portion of the model. This fracture energy was computed for the 3-D granite models to quantify the energy necessary to fracture the material under various loading conditions.

Figure 10 shows the fracture energy per unit area of fractured material for all the 3-D granite models. As the wear flat grows in size, more energy is required to fracture the rock. The energy required trends linearly with increased wear flat size. The pressurized models exhibit similar behavior, but with higher fracture energy required and more damaged area corresponding to a larger crush zone than the models without confining pressure. Within the pressure models, the wear flats all have higher fracture energies than the sharp cutter, with the small wear flat having the highest fracture energy and fracture area. We see that the large wear flat has a lower fracture energy than the sharp cutter in the no confining pressure case but in the confining pressure the large wear flat has a higher fracture energy than the

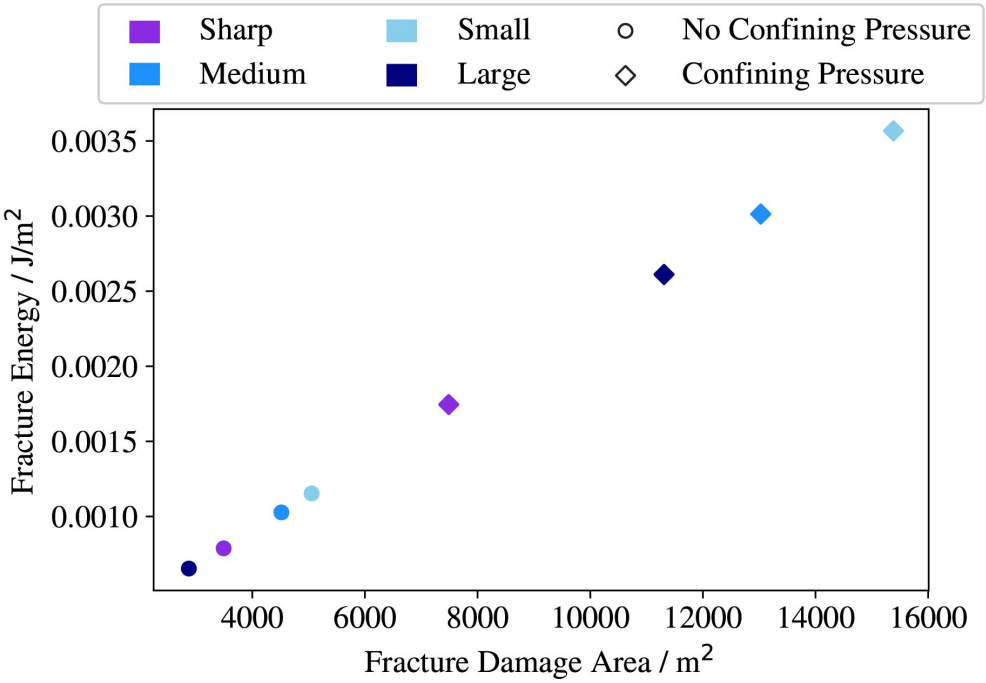

Figure 10: Comparison of fracture energy per unit area for the 3-D granite wear flat models, circles show no confining pressure models, diamonds show confining pressure models.

sharp. The models without confining pressure have a direct correlation to the cutting forces but the confining pressure models do not follow the same trend. This discrepancy in trend reinforces that the cutting dynamics are more complicated at downhole pressures and that increasing wear on a cutter does not necessarily correlate to immediate cutting degradation.

5. Discussion

Our modeling and simulation results provide a cohesive picture of the PDC rock cutting process. Our results indicate that slower cutter velocities and smaller depths of cut lead to lower overall cutting forces, while higher cutter velocities and larger depths of cut lead to higher cutting forces. When confining pressure is applied, we find that cutting forces increase and the displacement required to reach peak cutting force is greater than that required in the non-pressure models.

In Figure 11a, b, and c, we compare the final states of the 2-D models without confining pressure to make a qualitative assessment of the observed fracture patterns. Here we visualize the non-dimensional damage from 0.7 to 1, which shows a range of damage from heavily damaged bonds between elements to full fracture i.e. no connection between elements. The results illustrated in Figure 11 assume a cutter velocity of 4 m/s. As the depth of cut increases, the size of the generated rock fragments increases. This is accompanied by an increase in the damaged area of rock. The rock fragments accelerate away from the cutter after being fractured. Due to the back rake angle and the chamfer on the PDC cutter, some fragments are able to escape behind the cutter as it moves. In a geothermal drilling scenario, the presence of fluid in the drill column would slow the ejected fragments.

Figure 11(d, e, f) shows the final states of the pressurized 2-D models at a velocity of 4 m/s. For each case, the addition of the confining pressure results in a build up of fragmented rock in front of the cutter. The amount of built up rock fragments is proportional to the depth of cut. The build up of rock fragments in front of the cutter is seen in geothermal drilling and is referred to as bit balling. An important aspect of our models to note is that confining pressure is continuously applied normal to the face of the element where the boundary condition is imposed. As the simulation progresses, these elements are moved by the PDC cutter but retain the pressure boundary condition acting normal to the element face. This may have a minor effect on the simulated results. The pressurized models result in rock fragments

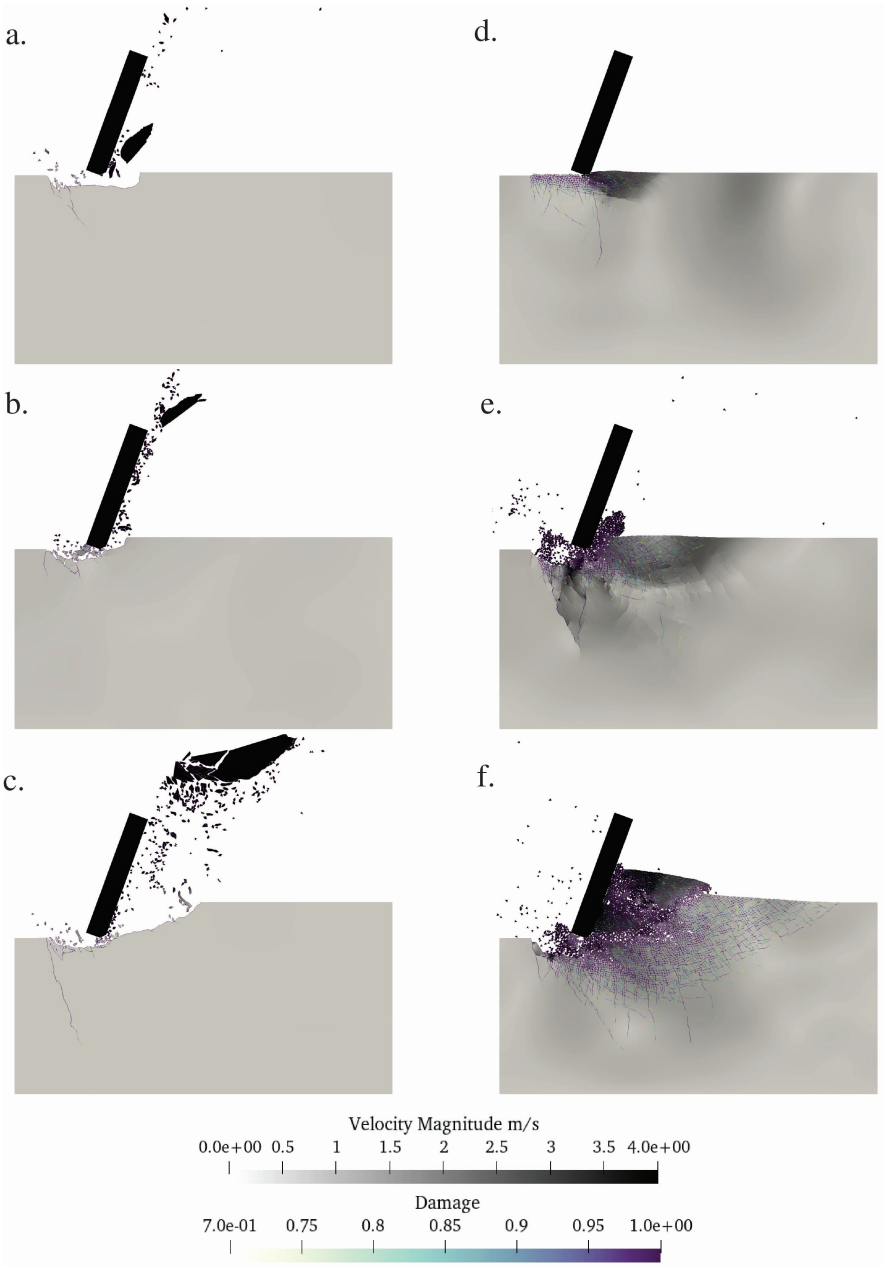

Figure 11: Snapshots of the 2-D, 4 m/s cutter velocity cases for no confining pressure (a, b, c) and confining pressure (d, e, f) cases. a.) shows 0.3 mm cut, b.) shows 1.2 mm cut, c.) shows 3.6 mm cut, d.) shows 0.3 mm cut pressure case, e.) shows 1.2 mm cut pressure case, and f.) shows 3.6 mm cut pressure case. Each model shows the velocity in the cutter and specimen as well as the damage, showing only damage values between 0.7 to 1, where 1 is fully damaged

that are primarily generated by shear damage. The rock fragments produced during pressurized cutting are typically smaller than those produced with no confining pressure.

When examining the 3-D results, we can explore the fracturing of the rock around the PDC cutter. In a geothermal drilling scenario, the target rock is heterogeneous with varying grain, mineral composition, and structure. Our models assume a homogeneous rock material for simplicity. However, in our numerical models, homogeneous rock does not break symmetrically, in part due to the randomization of the mesh. As our mesh size is the same order as the grain size, we are somewhat closely replicating the effects of grain size on the cutting process. Figure 12 shows two views temporal evolution of the 3-D model without confining pressure. As the cutter advances, the rock breaks and forms a crush zone around the bottom of the cutter as in [11]. Once developed, the crush zone does not extend deeper with time. The surface of the specimen fragments into thin, sheet-like chips, that are then further displaced by rock fragments moving upwards along the face of the cutter. This is similar to the brittle fragmentation we see in 2-D, where large rock fragments are created by the cutter. The distribution of the stress and the randomness of the mesh lead to an unevena distribution of fragment size parallel to the cutting face. Similar to the 2-D models with no confining pressure, fragments are created due to shear failure with some small regions of tensile failure.

In Figure 13 of the confining pressure model, we see a larger crush zone (both vertically and horizontally) when compared to the model with no confining pressure. However, there is much less build up of fragmented rock in front of the cutter. Only at the end of the simulation does a small mound of fragments start to build up in front of the cutter. The build up we do see has a higher velocity compared to the model without confining pressure. This lack of build up is likely due to the effect of the vertical component of pressure hindering the ability of the fragments to escape upwards. Again, shearing is the primary mode of failure with very little tensile failure occurring in the model.

When we compare our 3-D models to experimental results of PDC cutters, both with and without confining pressures, we find good agreement. [28, 29] conducted laboratory experiments of PDC cutting on sandstone with and without confining pressure. In both cases, they classified the sizes of rock cuttings and found that more large-sized rocks chips (>2 mm) are created during cutting without confining pressure, and more small-sized rock chips

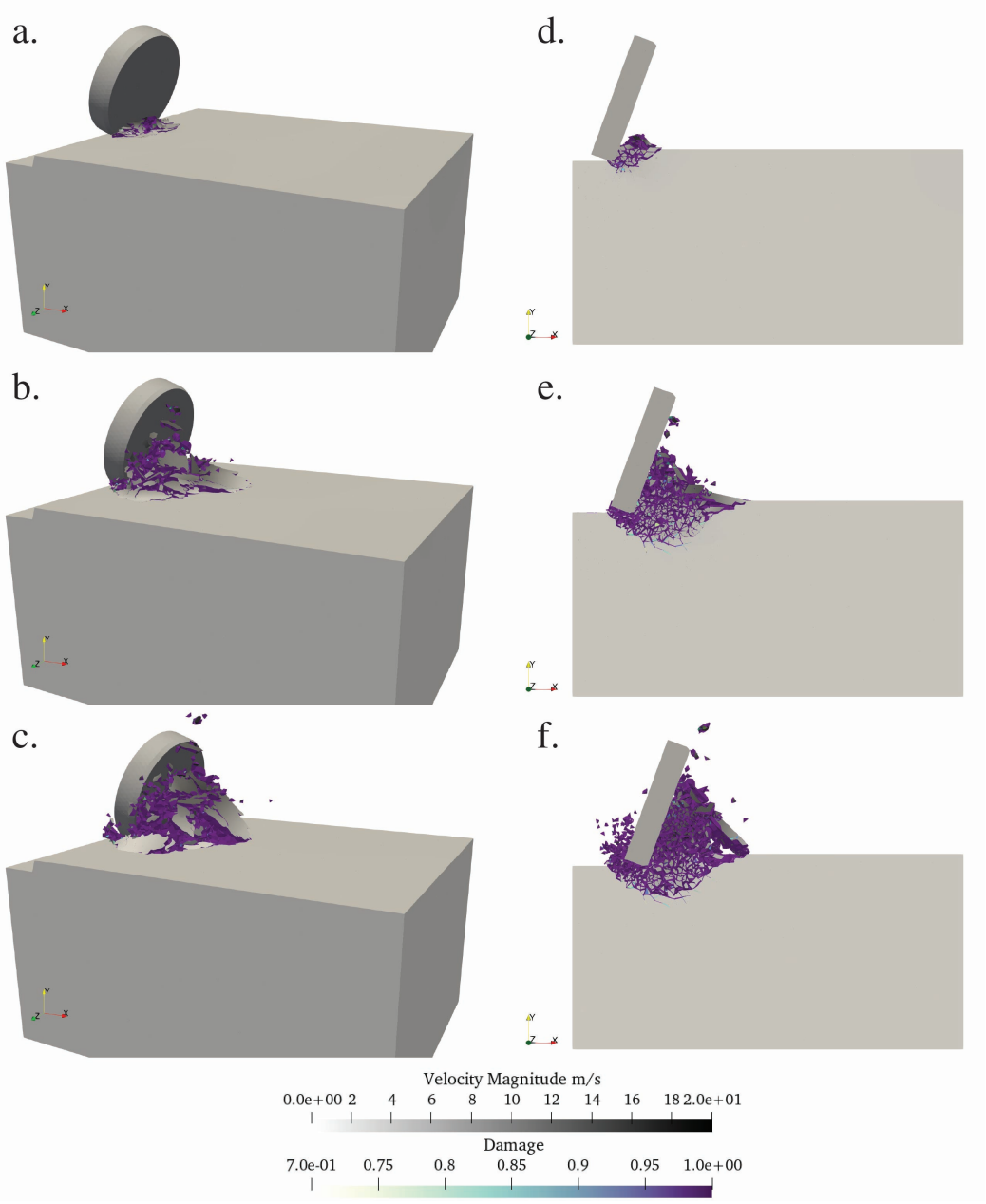

Figure 12: Three snapshots of the 3-D no confining pressure, 1.2 mm cut depth, 4 m/s cutter velocity model. a.), b.), and c.), show an angled full view, with d.), e.), and f.) showing a slice through the middle of the model. Each model shows the velocity of the cutter and specimen as well as the damage, showing damage values between 0.7 to 1

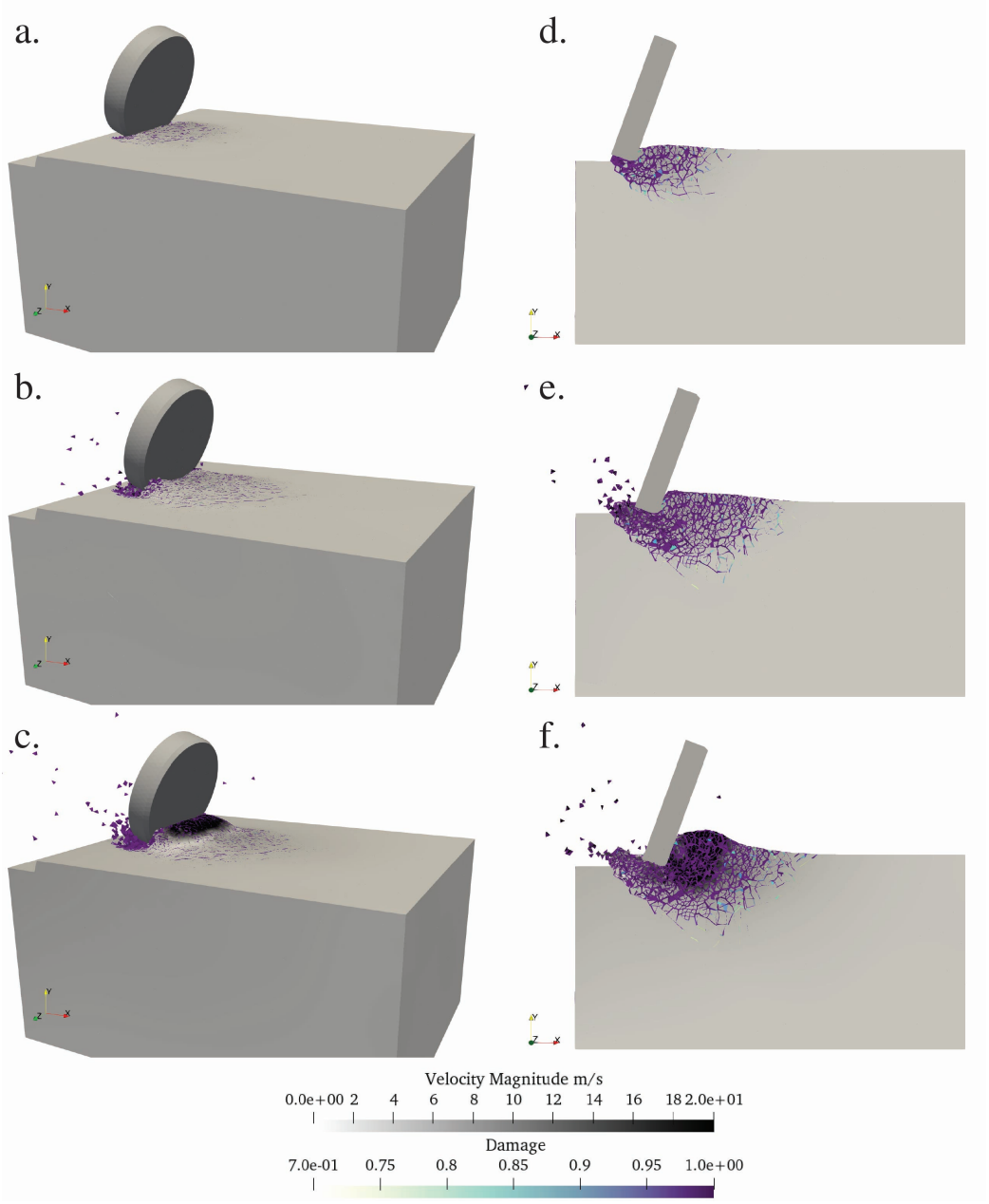

Figure 13: Three snapshots of the 3-D confining pressure, 1.2 mm cut depth, 4 m/s cutter velocity model. a.), b.), and c.), show an angled full view, with d.), e.), and f.) showing a slice through the middle of the model. Each model shows the velocity of the cutter and specimen as well as the damage, showing damage values between 0.7 to 1

(<0.3 mm) are created when cutting under confining pressure. We qualitatively observe similar rock fragment size distributions in our confined and unconfined 3-D models. Additionally, [29] observed the formation of flake-like chips during cutting without confining pressure, this phenomenon is observed in our models as well (see Figure 13b and c). The similarities between experimental results and our models indicate that our models are replicating PDC cutter-rock interactions observed in the laboratory.

The various wear flat models produce different fracture patterns (Figure 14. Using the same metric of damage as previous sharp cutter models (0.7 to 1), we see much deeper penetration of damage and fracture, reaching all the way to the bottom of the 20 mm box in Figure 14d, e, and f. This suggests that the wear flat has a different force on the block than the sharp cutter, which is able to shear the top of the rock. This observation is corroborated by Figure 7, which shows the differences in cutting forces. In general with a wear flat, there is a smaller contact area on the cutter as the contact area is no longer a semicircle and is now bisected by the wear flat. As the top of the cutter is at the same position, the contact area has thus decreased. We see the largest accumulation of cutting fragments in the smallest wear flat case, as well as a larger crush zone than the other wear flats, as the small wear flat has the largest cutting area comparatively. The larger crush zone seen in the wear flat models may be a result of the different contact area geometry than that of the sharp cutter. The wear flat models have a larger cutting edge than the sharp due to the wear pattern, this geometry change could be why there is a larger proportion of damage downwards and larger corresponding crush zone. However, this does not mean that worn cutters are more efficient for cutting.

When considering the observed damage types and their associated fracture energies we see a pattern emerge. PDC cutter-rock interactions are dominated by shear damage. This means that, as the cutter drags over the rock surface, the rock is being crushed by the cutter and pushed into the intact rock to further damage it. In the no confining pressure case this varies slightly by having larger amounts of tensile damage. The tensile damage is evident in the sheet-like fragments of rock that flake off as the PDC cutter moves forward. This damage mechanism is not present in the pressurized models due to the force applied on the rock surface. The required fracture energy increases when comparing a model without confining pressure to a corresponding pressurized model. This increase is in part due to the increase in fracture area that we see with the pressure models from Figures 13

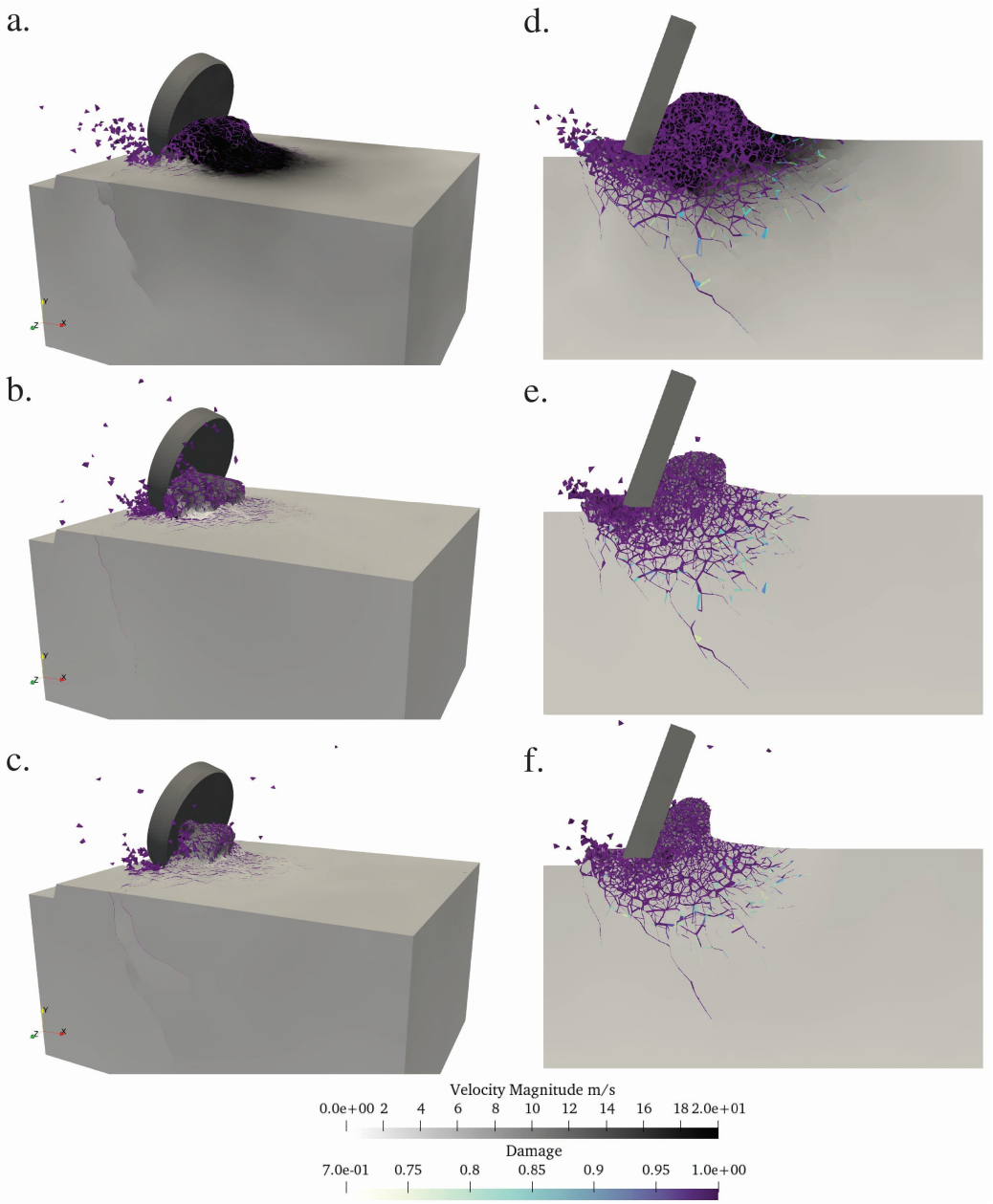

Figure 14: Comparison of wear flats in 3-D and as cross-sections, a.) and d.) are the small wear flat, b.) and e.) are the medium wear flat, c.) and f.) are the large wear flat. Each model shows the velocity in the cutter and specimen, and damage.

and 14. The increase of fracture energy and cutting force when we transition to models with confining pressure has implications for drilling efficiency as well.

A way of calculating cutting efficiency is a comparison between the work done by the cutter and the fracture energy. For this efficiency proxy, we calculated the work done by the cutter at the peak cutting force and calculate the fracture energy at that same point and then divide by a meter to get a dimensionless efficiency. This point is theoretically the least efficient for the cutter, i.e. when the most work is being done, but provides a conservative value for the efficiency. We computed the efficiency for the best and worst case scenarios, the sharp cutter, small wear flat, and large wear flat under confining pressure, respectively. The sharp cutter has a value of 24,641 while the large wear flat has a value of 15,384 and the small wear flat has a value of 15,714. Both the wear flats have a lower value than the sharp cutter, meaning they are less efficient at cutting. However, there is not a large difference between the small and large wear flats meaning that once the cutter is worn, the efficiency drops but does not continue dropping with more wear.

Based on the previous determination of fracture energy, we can calculate an estimate of fracture energy required for the whole drill bit. By multiplying the fracture energy required by one cutter by the number of cutters on the bit and the circumference of the drill bit for a revolution, we get an estimate for total fracture energy done by a drill bit. Assuming 6 blades on a 8.5 inch drill bit with 8 cutters per blade, for a sharp cutter under confining pressure, with a displacement of 6 mm we get a fracture energy of 9.5 J/m^2. In contrast, for a small wear flat under confining pressure we get a value of 18.8 J/m^2, nearly double that of the sharp cutter. This increase in fracture energy for small wear, coupled with the higher cutting force that we find as well, may explain the drastic drop in ROP found in drilling operations for small wear flats.

6. Conclusions

This work studied PDC cutter-rock interactions using HOSS in both 2D and 3D, with a range of depths of cut and cutter velocities. We replicated the magnitude of cutting forces observed in experimental scratch tests with HOSS. In 2D, increasing depth of cut increases the cutting force. Increasing the velocity of the cutter, however, greatly increases the cutting force while simultaneously lowering the time in contact with the rock. Incorporating a

confining pressure representative of geothermal drilling conditions leads to increases in both cutting force and the time in contact for the cutter. In addition, the confining pressure leads to a different distribution of rock fragment sizes, with fewer large rock fragments occurring and more sustained fragment build up on the cutter face. When pressurized, the rock cutting process is dominated by shear damage, but in cases without confining pressure tensile damage leads to flaking of the rock. The fracture energy required to completely damage the rock increases linearly with increasing wear flat size and with confining pressure. We find that the smallest wear flat size leads to the highest cutting forces and fracture energy, which could explain the drop in ROP seen in drilling operations. We demonstrate that HOSS is a tool to model this type of rock deformation and fracture and can help explain phenomena experienced during geothermal drilling operations.

7. Acknowledgments

This research used resources provided by the Los Alamos National Laboratory Institutional Computing Program, which is supported by the U.S. Department of Energy National Nuclear Security Administration under Contract No. 89233218CNA000001. Los Alamos National Laboratory is operated by Triad National Security, LLC, for the National Nuclear Security Administration of U.S. Department of Energy (Contract No. 89233218CNA000001). The views expressed herein do not necessarily represent the views of the U.S. Department of Energy of the United States Government. This document has been assigned a release number LA-UR-24-22288.

8. Declarations

- Funding - This work is supported by Department of Energy DOE Geothermal Technologies Office (GTO) – Geothermal Limitless Approach to Drilling Efficiencies (GLADE; DE-EE0010444) led by Oxy USA, Inc. This work was supported by the U.S. Department of Energy, Office of Science, Office of Basic Energy Sciences, Geosciences Research Program under Award Number (DE-SC0001048).

- Competing interests - The authors declare no competing interests.

- Author contribution - All authors contributed to the study conception and design. Numerical modeling, data collection and analysis were

performed by E. Heilman. The first draft of the manuscript was written by E. Heilman and all authors commented on previous versions of the manuscript. All authors read and approved the final manuscript.

References

[1] R. Dwivedi, R. Goel, V. Prasad, A. Sinha, Thermo-mechanical properties of indian and other granites, International Journal of Rock mechanics and mining Sciences 45 (3) (2008) 303–315.

[2] W. Kumari, P. Ranjith, M. Perera, S. Shao, B. Chen, A. Lashin, N. Al Arifi, T. Rathnaweera, Mechanical behaviour of australian strathbogie granite under in-situ stress and temperature conditions: An application to geothermal energy extraction, Geothermics 65 (2017) 44–59.

[3] P. Chen, X. Dai, F. Shao, E. Ozbayoglu, W. Liu, J. Wang, Review of pdc cutter–rock interaction: Methods and physics, Geoenergy Science and Engineering (2023) 211995.

[4] W. Liu, H. Deng, X. Zhu, K. Deng, The pdc cutter-rock interaction behavior in rock cutting: A review, Geoenergy Science and Engineering (2023) 212168.

[5] P. S. Dougherty, R. Pudjoprawoto, C. F. Higgs III, Bit cutter-on-rock tribometry: Analyzing friction and rate-of-penetration for deep well drilling substrates, Tribology International 77 (2014) 178–185.

[6] Y. Yang, C. Zhang, M. Lin, L. Chen, Research on rock-breaking mechanism of cross-cutting pdc bit, Journal of Petroleum Science and Engineering 161 (2018) 657–666.

[7] K. Pierce, B. Livesay, A study of geothermal drilling and the production of electricity from geothermal energy, Tech. rep., Sandia National Lab.(SNL-NM), Albuquerque, NM (United States) (1994).

[8] F. Dupriest, S. Noynaert, Drilling practices and workflows for geothermal operations, in: SPE/IADC Drilling Conference and Exhibition, SPE, 2022, p. D021S015R001.

[9] F. E. Dupriest, S. F. Noynaert, Continued advances in performance in geothermal operations at forge through limiter-redesign drilling practices, in: SPE/IADC Drilling Conference and Exhibition, SPE, 2024, p. D031S024R002.

[10] M. C. Jaime, Y. Zhou, J.-S. Lin, I. K. Gamwo, Finite element modeling of rock cutting and its fragmentation process, International Journal of Rock Mechanics and Mining Sciences 80 (2015) 137–146.

[11] Z. Fu, M. Tergeist, A. Kueck, G.-P. Ostermeyer, Investigation of the cutting force response to a pdc cutter in rock using the discrete element method, Journal of Petroleum Science and Engineering 213 (2022) 110330.

[12] E. E. Knight, E. Rougier, Z. Lei, B. Euser, V. Chau, S. H. Boyce, K. Gao, K. Okubo, M. Froment, Hoss: an implementation of the combined finite-discrete element method, Computational Particle Mechanics 7 (2020) 765–787.

[13] B. Euser, E. Rougier, Z. Lei, E. E. Knight, L. P. Frash, J. W. Carey, H. Viswanathan, A. Munjiza, Simulation of Fracture Coalescence in Granite via the Combined Finite–Discrete Element Method, Rock Mechanics and Rock Engineering 52 (9) (2019) 3213–3227. doi:10.1007/s00603-019-01773-0.
URL http://link.springer.com/10.1007/s00603-019-01773-0

[14] S. Boyce, Z. Lei, B. Euser, E. E. Knight, E. Rougier, J. C. Stormont, M. M. Reda Taha, Simulation of mixed-mode fracture using the combined finite–discrete element method, Computational Particle Mechanics 7 (5) (2020) 1047–1055. doi:10.1007/s40571-020-00341-6.
URL https://link.springer.com/10.1007/s40571-020-00341-6

[15] J. Morris, S. Johnson, Dynamic simulations of geological materials using combined fem/dem/sph analysis, Geomechanics and Geoengineering: An International Journal 4 (1) (2009) 91–101.

[16] O. K. Mahabadi, A. Lisjak, A. Munjiza, G. Grasselli, Y-geo: new combined finite-discrete element numerical code for geomechanical applications, International Journal of Geomechanics 12 (6) (2012) 676–688.

[17] M. Mohammadnejad, D. Fukuda, H. Liu, S. Dehkhoda, A. Chan, Gpgpu-parallelized 3d combined finite–discrete element modelling of rock fracture with adaptive contact activation approach, Computational Particle Mechanics 7 (2020) 849–867.

[18] A. Munjiza, The combined finite-discrete element method, Wiley, Hoboken, NJ, 2004.

[19] A. A. Munjiza, E. E. Knight, E. Rougier, Computational mechanics of discontinua, Wiley series in computational mechanics, Wiley, Chichester, West Sussex, U.K, 2012.

[20] A. A. Munjiza, E. Rougier, E. E. Knight, Large strain finite element method: a practical course, Wiley, Chichester, West Sussex, UK, 2015.

[21] E. Rougier, A. Munjiza, N. W. M. John, Numerical comparison of some explicit time integration schemes used in dem, fem/dem and molecular dynamics, International Journal for Numerical Methods in Engineering 61 (6) (2004) 856–879. arXiv:https://onlinelibrary.wiley.com/doi/pdf/10.1002/nme.1092, doi:https://doi.org/10.1002/nme.1092.
URL https://onlinelibrary.wiley.com/doi/abs/10.1002/nme.1092

[22] B. S. Tatone, G. Grasselli, A calibration procedure for two-dimensional laboratory-scale hybrid finite–discrete element simulations, International Journal of Rock Mechanics and Mining Sciences 75 (2015) 56–72.

[23] P. Bésuelle, J. Desrues, S. Raynaud, Experimental characterisation of the localisation phenomenon inside a vosges sandstone in a triaxial cell, International Journal of Rock Mechanics and Mining Sciences 37 (8) (2000) 1223–1237.

[24] T. Richard, F. Dagrain, E. Poyol, E. Detournay, Rock strength determination from scratch tests, Engineering Geology 147 (2012) 91–100.

[25] X. Zhu, Z. Dan, Numerical simulation of rock breaking by pdc bit in hot dry rocks, Natural Gas Industry B 6 (6) (2019) 619–628.

[26] J. Moore, S. Simmons, J. McLennan, C. Jones, G. Skowron, P. Wannamaker, G. Nash, C. Hardwick, W. Hurlbut, R. Allis, et al., Utah

forge: Phase 2c topical report, Tech. rep., USDOE Geothermal Data Repository (United States); Energy and Geoscience ... (2019).

[27] Y. Li, Z. Chen, Y. Ye, Y. Yang, Combined finite-discrete element method for modeling the interaction between single pdc cutter and brittle rock, Journal of Petroleum Science and Engineering 207 (2021) 109133.

[28] W. Liu, H. Deng, X. Zhu, R. Li, C. He, Experimental study of the rock cutting mechanism with pdc cutter under confining pressure condition, Rock Mechanics and Rock Engineering 56 (10) (2023) 7377–7396.

[29] W. Niu, H. Liao, H. Wang, X. Pei, Y. Shi, J. Niu, Analyzing the performance of single-cutter cutting rock under bottom-hole pressure conditions, Geoenergy Science and Engineering 233 (2024) 212435.